

Journal of Materials Chemistry A

Accepted Manuscript



This is an *Accepted Manuscript*, which has been through the Royal Society of Chemistry peer review process and has been accepted for publication.

Accepted Manuscripts are published online shortly after acceptance, before technical editing, formatting and proof reading. Using this free service, authors can make their results available to the community, in citable form, before we publish the edited article. We will replace this *Accepted Manuscript* with the edited and formatted *Advance Article* as soon as it is available.

You can find more information about *Accepted Manuscripts* in the [Information for Authors](#).

Please note that technical editing may introduce minor changes to the text and/or graphics, which may alter content. The journal's standard [Terms & Conditions](#) and the [Ethical guidelines](#) still apply. In no event shall the Royal Society of Chemistry be held responsible for any errors or omissions in this *Accepted Manuscript* or any consequences arising from the use of any information it contains.

ARTICLE

Magnetic-Field-Assisted Aerosol Pyrolysis Synthesis of Iron Pyrite Sponge-like Nanochain Networks as Cost-Efficient Counter Electrode in Dye-sensitized Solar Cell

Cite this: DOI:
10.1039/x0xx00000x

Received 00th January 2012,
Accepted 00th January 2012

DOI: 10.1039/x0xx00000x

www.rsc.org/

Zhanhua Wei^a, Yongcai Qiu^a, Haining Chen^a, Keyou Yan^a, Zonglong Zhu^a, Qin Kuang^a and Shihe Yang^{*a}

Aerosol pyrolysis of $\text{Fe}(\text{CO})_5$ in an atmosphere of sulfur vapor under magnetic field is shown to controllably produce iron pyrite (FeS_2) three-dimensional nanochain networks. The formation processes of the FeS_2 nanochain networks is systematically studied: (1) thermal decomposition of $\text{Fe}(\text{CO})_5$ followed by Fe nanoparticle assemble into one-dimensional chains and then three-dimensional networks under magnetic field, and (2) subsequent sulfurization in sulfur vapor atmosphere to form a sponge-like thin film of FeS_2 nanochain networks. Control experiment performed in the absence of magnetic field yielded randomly packed FeS_2 nanoparticles, rather than the inter-connected nanochain networks. The nanochain networks and their surfactant-free surfaces brought about by our new synthesis will enable a host of photoelectric applications. For example, when used as counter electrode for dye-sensitized solar cell, the FeS_2 nanochain networks are almost as efficient as noble Pt, and more impressively, their catalytic activity faded by only 8% after above 2000 cycles. This work opens up fresh opportunities to make smart use of earth-abundant materials in areas of sustainable energy and environment.

Introduction

Pyrite ($\beta\text{-FeS}_2$), the so-called fool's gold, is attracting growing interest for the next generation photovoltaics due mainly to its earth-abundance, low-cost and nontoxicity, coupled with a number of desirable properties including an exceptionally large optical absorption coefficient ($\alpha > 10^5 \text{ cm}^{-1}$ in the visible light region), a sizable minority carrier diffusion length (100-1000 nm) and an ideal band gap (0.95 eV).¹⁻¹¹ The classical synthesis of FeS_2 nanoparticles is exemplified by the hot-injection method (an organic solution process)^{12, 13} giving rise to FeS_2 nanocrystals with various morphologies such as nanowires, nanocubes and nanosheets.¹⁴⁻¹⁶ However, the as-prepared FeS_2 nanoparticles were invariably coated with long alkyl chain surfactants, which were commonly considered to cause serious interfacial contact problems in thin film materials and thereby hinder the intended electronic and photoelectric applications. Therefore, new methods other than the conventional wet-chemical solution process are sorely needed for the preparation of surface clean pyrite nanoparticles that are inter-connected and can be assembled into a well-defined mesoscopic thin film.

One of the possible applications of such mesoscopic films is in dye-sensitized solar cells (DSSC).¹⁷⁻²³ A typical

configuration of DSSC consists of working electrode, electrolyte solution with a redox mediator and counter electrode. Counter electrode, as an indispensable part of DSSC, is bifunctional: extracting electrons from the external circuit and catalyzing the reduction of I_3^- . Typically, fluorine doped tin oxide glass (FTO) loaded with noble metal platinum is used as standard counter electrode in DSSC. Although Pt has excellent catalytic activity for the reduction of I_3^- in DSSC, it is scarce and expensive, thus unsuitable for the industrial development. Extensive efforts have been made to exploit new materials as counter electrodes for DSSC, such as carbon materials (graphene, carbon nanotubes),²⁴⁻²⁶ conductive polymers,^{27, 28} and transition metal compounds (nitrides, carbides, oxides, sulphides and selenides).²⁹⁻³³ However, these materials still suffer from low efficiency, poor thermal stability and corrosion resistance. Therefore, the development of Pt-free counter electrodes for DSSC using cheap and earth-abundant materials remains an outstanding goal. Very recently, surfactant coated iron pyrite nanoparticles were prepared by the conventional hot-injection method, and when used as counter electrodes for DSSC after removing the surfactants, promising results were obtained.³⁴ Further performance improvements are expected if

the surfactants are entirely avoided and the nanoparticles are better assembled in the synthesis process.

Herein, we report a scalable and continuous aerosol pyrolysis preparation route for pure and clean pyrite three-dimensional (3D) nanochain networks. Our method is based on magnetic field assisted assembly of *in-situ* generated Fe nanoparticles from Fe(CO)₅ acetone aerosol, and subsequent sulfurization in sulfur vapor atmosphere to form the FeS₂ nanosponge. The main advantageous features of our synthesis method are: (1) The product has a sponge-like 3D nanochain network morphology, which is beneficial to facile charge transport; (2) The nanoparticle surfaces are clean and free of surfactants, a feature which is essential for fast charge transfer kinetics; (3) Above all, it is a simple and mass production process for a low-cost material. Indeed, when employed as counter electrode for DSSC, the as-prepared pyrite nanochain network is nearly as efficient as noble Pt and the excellent catalytic activity exhibited no significant decay after above 2000 cycles.

Experimental

Preparation of FeS₂ sponge-like 3D nanochain network

The setup of pyrolysis synthesis is schematically shown in Figure 1A and was installed in a fume hood. Iron pentacarbonyl precursor (Fe(CO)₅, 0.2 M) was prepared by mixing 1 mL of Fe(CO)₅ with 37 mL of acetone. After nitrogen-purging, the precursor solution was pumped into a home-made ultrasonic atomizer (1.7 MHz). The precursor solution was atomized into aerosol, which was carried by N₂ gas into a customized three-neck flask. The bottom of the flask was thermally blown into a flat shape to optimize the contact with a heating plate. The pyrolysis reactions were confined in the flask, which was kept at 400 °C by the heating plate (the magnetic stirring function was turned off and the magnetic-field intensity was measured to be ~1.5 mT at the reactor) or a heating mantle (no magnetic stirring function). To synthesize FeS₂ products, 0.2 g of sulfur was loaded into a semi-closed container, which was located at the bottom but off center of the flask. The final product was harvested by a filter paper which was placed on one of the flask necks.

Preparation of FeS₂ and Pt counter electrodes

First, the as-prepared FeS₂ nanochain network powder was dispersed in isopropanol (IPA) to prepare a painting suspension (2 mg mL⁻¹), and then drop-casted on a FTO glass to form a thin film. The thickness was adjusted by repeating the coating process. In addition, the film was compressed (50 MPa, 1 min) to further promote the inter-particles connection.

Pt counter electrode was prepared according to the well-documented thermal platinization: the Pt catalyst was deposited on an FTO glass by drop coating of H₂PtCl₆ solution (2 mg mL⁻¹, isopropanol), followed by heat treatment at 400 °C for 15 min.

Material characterization

Powder X-Ray diffraction (XRD) data was collected on an X'pert Pro (PANalytical) with Cu K α radiation. Brunauer-Emmett-Teller (BET) surface area was measured with Coulter SA 3100 Surface Area and Pore Size Analyzer. Morphologies of as-deposited FeS₂ thin film were directly examined on JEOL6700F Scanning electron microscope (SEM) at an accelerating voltage of 5 kV. Transmission electron microscope (TEM) and high resolution transmission electron microscope (HRTEM) observations were carried out on a JEOL 2010 transmission electron microscope operating at 200 kV. Film thickness was determined by a Tencor Alpha-Step 200 surface profiler system and confirmed by three consecutive measurements. Raman measurement was conducted with Renishaw 2000 laser Raman microscope equipped with a 514.5 nm 20 mW argon ion laser of 2 mm spot size for excitation. The magnetic field intensity was detected by F.W. BELL 4048 gauss meter.

Fabrication of DSSC

Firstly, active TiO₂ nanoparticles (~20 nm) and scattering TiO₂ microparticles (~400 nm) were prepared following a previous report.¹⁸ Films for solar cell test (photoanodes) were deposited by the screen printing method and carved into a circle (diameter of 5.5 mm). Post treatment included first calcination (450 °C, 30 min), TiCl₄ treatment (40 mM, 75 °C, 30 min) and second calcination (500 °C, 30 min). After the films were cooled down to about 80 °C, they were immersed into a 0.5 mM N-719 dye solution in a mixture of acetonitrile and tertbutyl alcohol (volume ratio, 1:1) and kept at room temperature for 20–24 h to ensure complete sensitizer uptake. Thereafter, the films were washed with ethanol and dried in air. The dye-coated electrodes were finally assembled into sandwich solar cells together with the platinum or FeS₂ counter electrodes, and sealed with a hot-melt gasket (25 μ m, Surlyn films 1702). A solution of 0.6 M BMII, 0.03 M I₂, 0.10 M guanidiniumthiocyanate and 0.5 M 4-tertbutylpyridine in a mixture of acetonitrile and valeronitrile (volume ratio, 85:15) was used as electrolyte, and was injected into the sealed cell through a pre-drilled hole by the vacuum-infusion method.

Evaluation of catalytic activity and solar cell performance

Cyclic voltammograms (CV) and Tafel curves were recorded with an electrochemical analyser (CHI660D, Chenhua, Shanghai). CV measurements were conducted in a three-electrode configuration with an argon-purged electrolyte solution (electrolyte: 10 mM LiI, 1 mM I₂ and 0.1 M LiClO₄ in acetonitrile) at a scan rate of 20 mV s⁻¹, a Pt wire counter electrode and a Ag/AgCl reference electrode. Symmetrical sandwich cells for Tafel polarization and electrochemical impedance spectroscopy (EIS) tests were fabricated by clamping two identical counter electrodes and sealing with a hot-melt gasket (50 μ m, Surlyn films). The light source (Newport solar simulator, model number 6255, 150 W Xe lamp, AM 1.5 global filter) was calibrated to 1 sun (100 mW cm⁻²) using a silicon reference solar cell equipped with KG-5 filter. A 5 mm diameter circular mask was used to define the

illumination area of the cells to be tested and block the reflecting light. J - V characteristic curves and EIS were recorded using an IM6x electrochemical workstation (ZAHNER-Elektrik GmbH & Co., KG, Germany). EIS was performed from 1 MHz to 50 mHz on symmetrical dummy cells (bias: 0 V), with the amplitude of the AC voltage was set at 10 mV. The EIS spectra were fitted by the Zview software.

Results and discussion

Preparation and characterization of FeS₂ sponge-like nanochain network

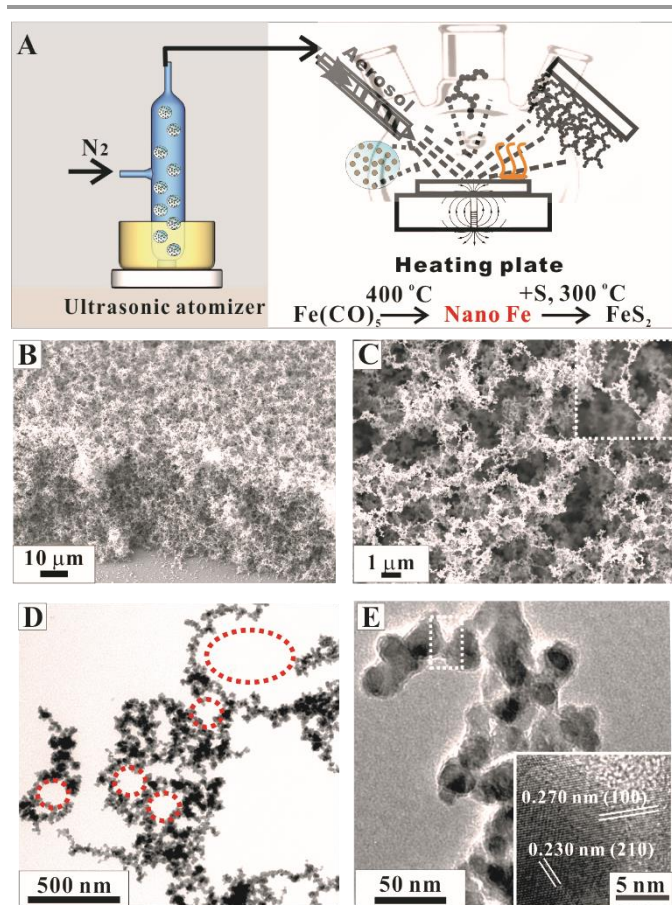


Figure 1. (A) Schematic diagram of magnetic field assisted aerosol pyrolysis preparation of FeS₂ nanochain network. Left: ultrasonic atomizer supplies Fe(CO)₅ acetone aerosol; Right: magnetic-field (1.5 mT) assisted aerosol pyrolysis, reactions and product collection. (B) Oblique and (C) top view SEM images of the as-prepared FeS₂ nanochain network. The inset in (C) is the corresponding enlarged SEM image. (D) TEM and (E) HRTEM images of the as-prepared FeS₂ nanochain assemblies.

As schematically illustrated in Figure 1A, Fe(CO)₅ aerosols are generated by an ultrasonic atomizer and then transported to the customized three-neck flask by N₂ carrier. Fe nanoparticles are immediately formed by thermal decomposition of Fe(CO)₅ and subsequently assembled into 1D nanochains mediated by the magnetic field. The Fe nanochains are then sulfurized in the presence of the hot sulfur vapor forming FeS₂ (see the experimental section and the following discussion for more details). A fluffy black powder is harvested by a filter paper

attached to one of the flask necks for further characterization and device assembly without extra purification steps.

Figure 1B and 1C show the SEM images of the as-prepared product, exposing a nice sponge-like morphology with numerous micrometer-sized pores. The high-magnification SEM image in Figure 1C reveals that the sponge-like structure is actually made up of 3D nanochain networks, in which the 1D nanochains are randomly interlaced with one another. More structural information is provided by TEM images Figure 1D and 1E. As indicated by red circles in Figure 1D, the pores are built from such nanochain networks whose basic morphology is still retained even after intense ultrasonic treatment in the TEM sample preparation. This implies that the connectivity of nanochains is numerous, branched and robust. Two factors can contribute to such a structurally firm mechanically stout connectivity. First, the nanochains have a zig-zag morphology at a small length scale but are branched at larger length scales as can be seen in Figure 1C and 1D. Second, the welding between primary nanoparticles inside nanochains can be directly observed from the TEM image in Figure 1E. Clearly seen in the inset of Figure 1E is a close-up of a welding-induced necking, which actually displays a coherent lattice fringe across the adjoining nanocrystals with a spacing of 0.270 nm corresponding to the (100) plane. The HRTEM image divulges that the primary nanoparticles are 10-20 nm in size and, aside from the (100) lattice fringe, the lattice fringe of (210) is also observed with a spacing of 0.230 nm. Of note, such a continuous chain network structure is preferable for the expeditious transport of elemental excitations such as charge carriers, heat, etc., a salient feature which is important for electrochemical catalysis as will be demonstrated below.

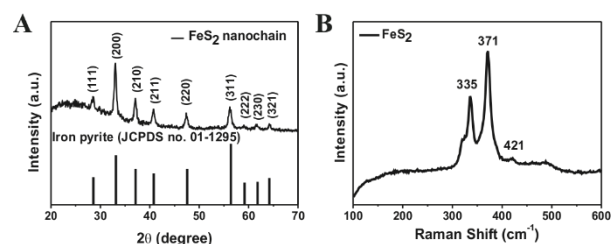


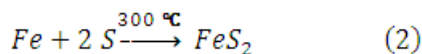
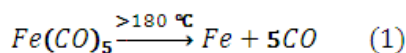
Figure 2. XRD and Raman characterization of the FeS₂ nanochain network. (A) XRD data shows perfect matching to the standard XRD pattern of iron pyrite (FeS₂); (B) Raman spectrum of the as-prepared FeS₂ nanochain network supports the pure pyrite phase.

To confirm the purity of FeS₂ phase, XRD and Raman spectroscopy were employed as independent crystallographic and spectroscopic probes, respectively. As shown in Figure 2A, the XRD pattern of the sample matches well with the standard pattern of pyrite phase (JCPDS no. 01-1295). Note that all the diffraction peaks are obviously broadened, indicating the nano-size of the crystallites. The crystallite size estimated from the broadening of the (200) peak by the Scherrer equation ($D = k\lambda/\beta\cos\theta$) is 15 nm, consistent with TEM observations. The Raman spectrum of the sample is shown in Figure 2B. Three feature peaks of pyrite located at 335 cm⁻¹ (strong), 371 cm⁻¹

(strong), and 421 cm^{-1} (weak) are clearly observed, and there are no measurable peaks of other phases such as marcasite (about 323 cm^{-1}). This verifies the pyrite phase of the as-prepared FeS_2 nanochain network and its phase purity.

Magnetic field induced assembly

The reactions involved in the synthesis of the FeS_2 nanochain network are given below:



The thermal decomposition of $\text{Fe}(\text{CO})_5$ (equation 1),³⁵⁻³⁷ and the magnetic field induced assembly of the nascent Fe nanoparticles and the like has been well-documented.³⁸⁻⁴² To ascertain the magnetic field induced assembly in our case, the synthesis was conducted by removing the S source but under otherwise identical reaction conditions. The resulting characterization data are presented in Figure S1, showing that the final product is still a sponge-like 3D nanochain network but in a Fe_3O_4 phase. Plausibly, the initial Fe nanosponge did form but was unstable in the air and hence oxidized to Fe_3O_4 . We can thus conclude that the magnetic field mainly directs the assembly of initial Fe nanoparticle formed due presumably to their large ferromagnetic moments. Figure 3A schematically illustrates the magnetic field induced process and the stepwise reactions (reaction 1 and 2). In general, each aerosol droplet is an independent reaction unit. On reaching the pyrolysis chamber at an elevated temperature, evaporation of acetone and decomposition of $\text{Fe}(\text{CO})_5$ takes place at the same time. Due to the combined effect of the magnetic field and the high temperature, the Fe nanoparticles are assembled and welded into nanochain networks, and subsequently transformed to the FeS_2 nanochains networks via sulfurization (equation 2). To vindicate the critical role of the magnetic field in the assembly process, we removed the magnetic field by switching the heating hotplate to a heating mantle while keeping other reaction conditions unchanged. In marked contrast, the resulting product contains no nanochain networks as shown in Figure 3B. Instead, the primary Fe nanoparticles tend to aggregate and melt together so as to minimize surface energy at the reaction temperature. After sulfurization, the final product became FeS_2 molten-nanoparticles. Therefore, the magnetic field has evidently played a critical role in assembling the observed nanochain networks by enhancing the dipole-dipole interactions amid the thermal motion and the random spatial distribution of the primary nanoparticles.

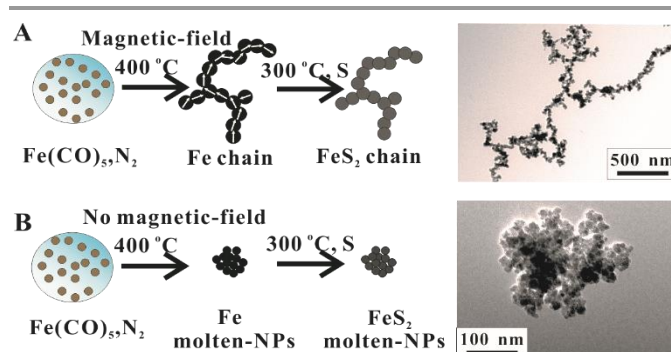


Figure 3. The formation process of the FeS_2 nanochain network. (A) Aerosol pyrolysis of $\text{Fe}(\text{CO})_5$, magnetic field assisted assembly, and reaction with S lead to the formation of the FeS_2 nanochain network; (B) Direct aerosol pyrolysis of $\text{Fe}(\text{CO})_5$ and reaction with S without magnetic field only produce FeS_2 molten-nanoparticles (the reaction conditions are the same as in (A) except for the absence of the magnetic field).

From TEM images in Figure 3, it is evident that the surface area of the nanochain network is larger than that of the molten-nanoparticles. Indeed, from BET measurements (see Figure S2), the specific surface area of the molten-nanoparticles is only about $37.70\text{ m}^2\text{ g}^{-1}$. By contrast, the as-prepared FeS_2 nanochain network has a relatively large BET surface area of $54.46\text{ m}^2\text{ g}^{-1}$. The smaller surface area of the FeS_2 molten-nanoparticles can be attributed to the melting aggregation process, in which the nanoparticles are fused together so as to minimize surface free energy. In contrast, the magnetic field guides the assembly process preferentially along the field direction, resulting in the higher specific surface area.

Catalytic activity of the FeS_2 sponge-like 3D nanochain network

The FeS_2 3D nanochain network is desirable for efficient charge transport and the surfactant-free mesoscopic surfaces are beneficial to electrochemical catalytic activity. For this purpose, we chose to evaluate its counter electrode performance in DSSC. The catalytic activity is studied together with control samples of molten-nanoparticles as well as the commonly used Pt electrode.

The FeS_2 nanochain network and molten-nanoparticles thin films were prepared by drop-casting method, followed by compression post treatment, which significantly improved the inter-particle connection and the overall thin film quality (see Figure S3 and S4). The Pt thin film was prepared by thermally platinizing a precursor film deposited with an H_2PtCl_6 IPA solution. For the clarity of presentation, the Pt counter electrodes are abbreviated as Pt-CEs, while the FeS_2 nanochain network and molten-nanoparticles counter electrodes are named as FeS_2 -chain-CEs and FeS_2 -MN-CEs, respectively. CV, Tafel and EIS measurements were performed to systematically investigate the catalytic activity of the FeS_2 electrodes in iodine/triiodine electrolyte.

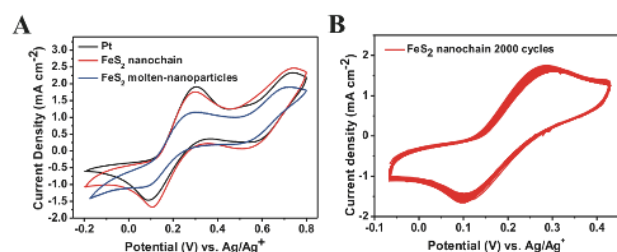
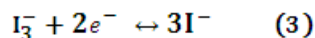


Figure 4. Performance evaluation of the FeS₂-chain-CEs by CV in a three-electrode configuration. (A) Cyclic voltammograms of Pt and FeS₂ counter electrodes (thickness: 4 μm, electrolyte: 10 mM LiI, 1 mM I₂ and 0.1 M LiClO₄ in acetonitrile, at a scan rate of 20 mV s⁻¹); (B) Long-term stability evaluation of FeS₂ nanochain in iodine electrolyte.

As described above, CV measurements were conducted in a three-electrode configuration with an argon-purged electrolyte solution. Figure 4A shows typical cyclic voltammograms of Pt and FeS₂ electrodes for iodine species (I₃⁻/I⁻). For all of the three counter electrodes, two pairs of redox peaks are observed; the peak at lower potential can be assigned to the redox pair of I₃⁻/I⁻ (equation 3), and that at higher potential to I₂/I₃⁻ (equation 4).



Two features of the CV curves are noteworthy. First, the FeS₂-chain-CEs display nearly the same overpotential and reversibility as that of the Pt-CEs, indicating the kinetic facility of the redox reaction of I₃⁻/I⁻ on their surfaces. Second, the redox peaks of the FeS₂-chain-CEs exhibit a current density as large as that of the Pt-CEs, while FeS₂-MN-CEs only show nearly half of the current density. To evaluate the long term stability of the FeS₂-chain-CEs, CV cycles up to 2000 are recorded. Remarkably, as shown in Figure 4B, little change in CV curve shape, redox peak positions and current densities have occurred, indicating the superior stability and catalytic activity of the FeS₂ thin films. As the catalytic activity of FeS₂-MN-CEs is too low, their stability was not tested further. One can conclude that the FeS₂-chain-CEs are as efficient and stable as Pt in catalyze the regeneration of I₃⁻/I⁻ species in the electrolyte.

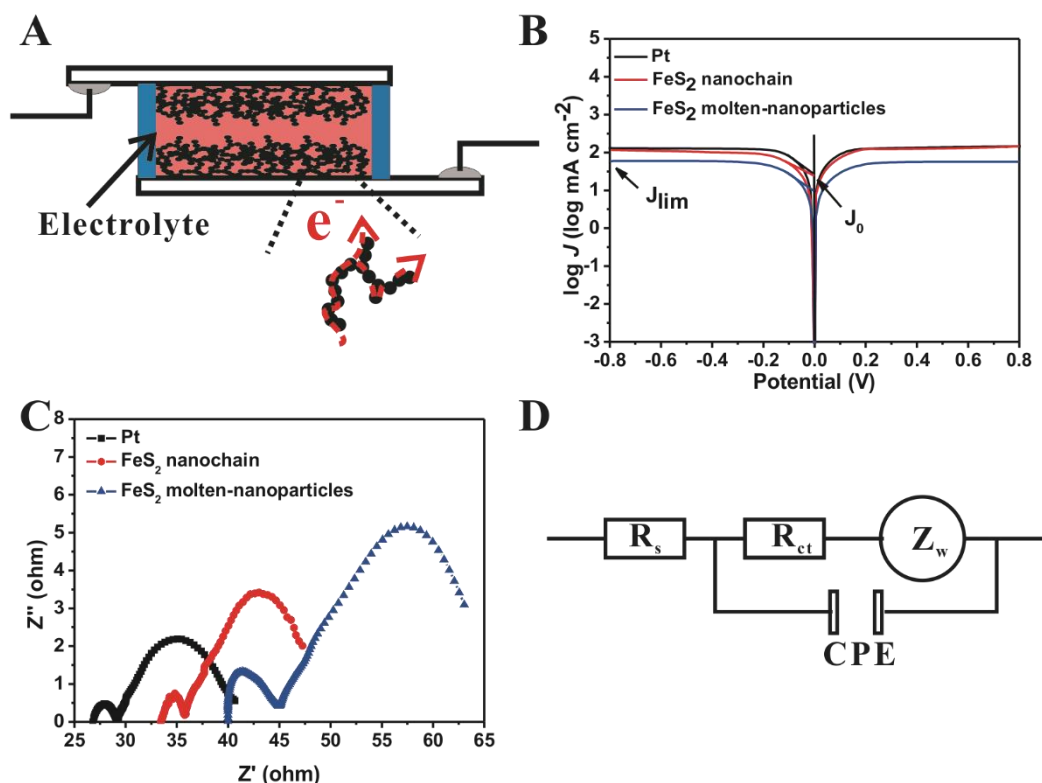


Figure 5. Performance evaluation of the FeS₂-chain-CEs by Tafel and EIS measurements in a symmetric cell. (A) Schematic diagram of a symmetric cell consist of two identical FeS₂-chain-CEs; (B) Tafel polarization curves at a scan rate of 20 mV s⁻¹; (C) EIS spectra of the corresponding symmetrical cells; and (D) EIS equivalent circuit of the symmetrical cells, R_s: the series resistance, R_{ct}: the charge transfer resistance, Z_w: Nernst diffusion impedance and CPE: constant phase angle element.

To further examine the catalytic activity, symmetrical cells made up of two identical electrodes were fabricated (see Figure 5A) for the Tafel and EIS measurements. Figure 5B shows the Tafel polarization curves of the Pt-CEs, FeS₂-chain-CEs and FeS₂-MN-CEs. Tafel polarization curve can be divided into

three zones, i.e., polarization zone (low potential, |U| < 120 mV, in general), Tafel zone (middle potential, with a sharp slope) and diffusion zone (high potential, horizontal section). In the diffusion zone, the intercept of cathodic branch with the Y-axis is defined as limiting current density (J_{lim}). It can be easily seen

that J_{lim} of FeS₂-chain-CE is comparable to Pt, reflecting FeS₂-chain-CE also allow high diffusion velocity of the redox couple. Second, the intersection of the cathodic branch in the Tafel zone at the equilibrium potential line can be considered as exchange current density (J_0). It can be indicated that FeS₂-chain-CEs exhibit similar (slight lower) J_0 with the Pt-CEs, which further confirms that FeS₂ nanochain and Pt have similar catalytic activity for I₃⁻ reduction. However, both of J_{lim} and J_0 of FeS₂-MN-CEs are lower than those of the Pt-CEs and FeS₂-chain-CEs, indicating a lower catalytic ability, this is probably because of the reduced surface area and lower charge transfer rate which can be directly reflected by EIS.

EIS Nyquist plots of the Pt-CEs, FeS₂-chain-CEs and FeS₂-MN-CEs in I₃⁻/I⁻ electrolyte are shown in Figure 5C, which all present two typical semi-circles. The corresponding equivalent circuit is schematized in Figure 5D. The high frequency intercept on the real axis represents the series resistance (R_s), the charge transfer resistance (R_{ct}) and constant phase angle element (CPE) are obtained by fitting the semicircle in the high frequency region (leftmost semicircle). The right-hand semicircle in the low-frequency range represents the Nernst diffusion impedance (Z_w) of the I₃⁻/I⁻ couples in the electrolyte. In general, R_{ct} indicates the catalytic property for I₃⁻/I⁻ electrolyte and J_0 varies inversely with R_{ct} according to equation 5.

$$J_0 = \frac{RT}{nFR_{ct}} \quad (5)$$

Where R is the gas constant, T is the absolute temperature, n is the number of electrons, and F is the Faraday constant. In Figure 5C, it is clear that the R_s of FeS₂-chain-CEs and FeS₂-MN-CEs is larger than that of Pt-CEs with the order of FeS₂-MN-CEs > FeS₂-chain-CEs, which may be due to the increasing contact resistance of FeS₂/FTO interface. As the FeS₂ thin film was prepared by drop-casting combined with compression post-treatment, in other word, no calcination process was used. Therefore, the FeS₂ thin films were not so firmly attached on FTO glass compared to the thermally platinizing ones (Pt-CEs). By fitting the EIS results, FeS₂-chain-CEs has similar R_{ct} (1.63 Ω cm²) to Pt (1.55 Ω cm²), yielding J_0 of 15.95 mA cm⁻² and 16.77 mA cm⁻², which is consistent with Tafel test results. However, the value of FeS₂-MN-CEs increases to 4.20 Ω cm², indicating a poor catalytic performance. Therefore, the EIS results have forcefully demonstrated that the FeS₂ nanochain thin films are as efficient as Pt in catalyzing reduction of the I₃⁻/I⁻ redox reaction, and are significantly more active catalysts than the FeS₂-MN-CE.

Solar cell performance

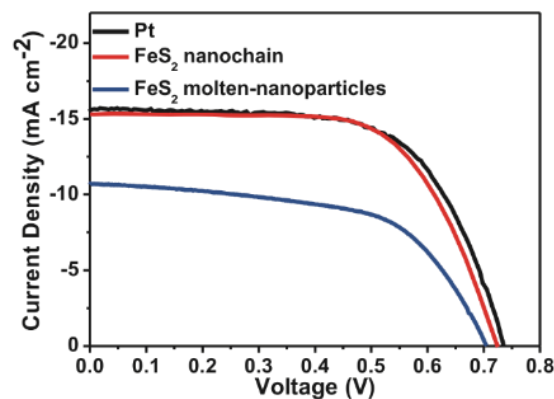


Figure 6. J - V curves of the DSSCs using Pt and FeS₂ as the counter electrodes.

To study performance of the FeS₂ counter electrodes in real operation, a series of DSSC devices were fabricated based on FeS₂-chain-CEs, FeS₂-MN-CEs and Pt-CEs and comparatively studied. Typical J - V curves of the different DSSCs are presented in Figure 6 and the detailed photovoltaic parameters are summarized in Table 1. First and foremost, the FeS₂-chain-CEs-DSSC have reached similar performance to the Pt-CEs-DSSC. More specifically, as a gold standard, the Pt-CEs-DSSC exhibited open-circle potential (V_{oc}) of 0.73 V, short-circuit photocurrent (J_{sc}) of 15.7 mA cm⁻², and fill factor (FF) of 0.66, yielding a photoelectric conversion efficiency (PCE) of 7.56%. In comparison, for the FeS₂-chain-CEs-DSSC, V_{oc} was 0.72 V, J_{sc} 15.3 mA cm⁻², and FF 0.65, corresponding to a PCE of 7.16%, quite close to that of the Pt-CE-DSSC. In sharp contrast, the FeS₂-MN-CEs-DSSC only showed a poor performance with a PCE of only 4.22%. These results indicate that the performance of FeS₂ nanochain network is a promising low-cost replacement for Pt as a counter electrode in DSSC, whereas the FeS₂ molten-nanoparticles are not even close, which highlights the superior charge transport brought about by the 3D interlacement of the magnetic field induced nanochain networks.

Table 1. Photovoltaic performance summary of DSSCs with the FeS₂ and Pt counter electrodes under AM 1.5 illumination at 100 mW cm⁻².

Solar cell	V _{oc} (V)	J _{sc} (mA cm ⁻²)	FF	PCE (%)
Pt-CEs	0.73±0.01	15.7±0.2	0.66±0.01	7.56±0.32
FeS ₂ -chain-CEs	0.72±0.01	15.3±0.1	0.65±0.01	7.16±0.25
FeS ₂ -MN-CEs	0.70±0.02	10.4±0.2	0.58±0.01	4.22±0.30

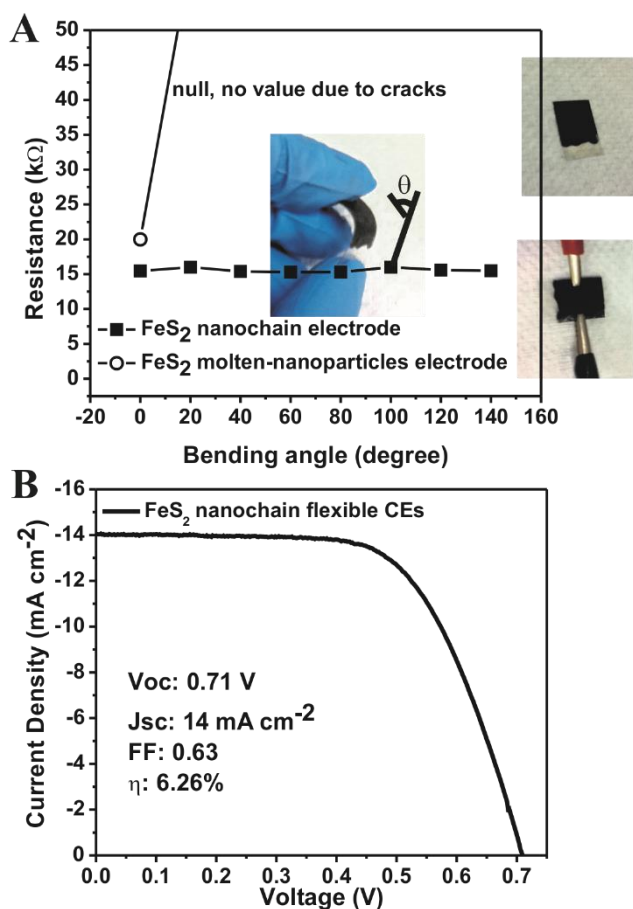


Figure 7. Performance evaluation of the FeS₂ nanochain network used as flexible counter electrode in DSSC. (A) Resistance-bending angle curves of thin films of the FeS₂ nanochain network and molten-nanoparticles on PET substrates (non-conductive); (B) DSSC performance with the FeS₂ nanochain network flexible CEs on PET-ITO substrates.

In addition to the high catalytic activity and the stable catalytic performance comparable to the Pt-CEs, the FeS₂ nanochain network has an added advantage of flexibility, which is essential for future large-scale roll-to-roll production. In order to demonstrate this feature, the FeS₂ nanochain network and the molten-nanoparticles thin films were firstly deposited on PET substrates (non-conductive side) by drop-casting combined compression methods, and then resistance-bending angle curves were recorded (see the optical images in Figure 7A for the setup) to evaluate the flexible conductivity

performance. As shown in Figure 7A, the FeS₂ molten-nanoparticles thin film has an initial resistance of about 20 kΩ, but when bended, it becomes non-conductive due to cracking. In contrast, the FeS₂ nanochain network thin film only shows a slight resistance variation (around 15 kΩ) even when it is bended by up to 140°.

As a preliminary demonstration of its use in flexible DSSC, the FeS₂ nanochain network thin film was deposited on a PET-ITO substrate and assembled into a DSSC device with a photoanode of N719-sensitized TiO₂ thin film on FTO glass, and the corresponding cell performance is presented in Figure 7B. Significantly, the DSSC based on the FeS₂ flexible counter electrode also achieves a considerably high PCE of 6.26%, which is only slightly lower than that with the FeS₂-chain-CEs on FTO glass (7.16%). Even this performance decrease is mainly due to the higher sheet-resistance of the PET-ITO substrate used in the flexible device, as found in previous reports.^{43, 44} Therefore, the ability to prepare the FeS₂ nanochain network thin films will allow high performance flexible DSSCs to be developed.

Conclusion

To sum up, magnetic field was judiciously utilized to assist pyrolysis preparation of 3D FeS₂ sponge-like nanochain network. The key role of the magnetic field is to guide the assembly of the precursor Fe nanoparticles generated *in-situ* by ultrasound assisted pyrolysis. The as-prepared FeS₂ nanochain network can maintain its morphology even after intense ultrasonic treatment. Compared to the molten nanoparticles (prepared without magnetic field), the 3D network features more efficient charge transport along the 1D nanochain structure. In addition, the clean mesoscopic surface due to the surfactant-free synthesis process is beneficial to optimize the electrocatalytic activity of the nanochain network. When used as counter electrode in DSSC, the FeS₂ nanochain network thin films were proven to be as effective as Pt for the electrocatalysis of (I₃⁻/I⁻). From the synthesis point of view, our strategy can be extended to prepare a family of oxide, sulphide, selenide and phosphide nanochain networks based on some earth-abundant magnetic elements (Fe, Mn, Co, Ni, etc.), which are promising for application in areas of energy and environments.

Acknowledgements

This work was supported by the HK-RGC General Research Funds (GRE No. HKUST 606511, 605710).

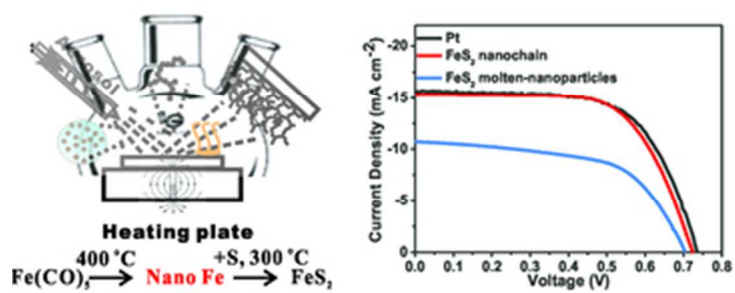
Notes and references

^a Department of Chemistry, Nano Science and Technology Program, The Hong Kong University of Science and Technology, Clear Water Bay, Kowloon, Hong Kong

Corresponding email: chsyang@ust.hk

Electronic Supplementary Information (ESI) available: control experiment results, BET analysis, preparation and characterization of FeS₂ thin film. See DOI: 10.1039/b000000x/

1. S. Seefeld, M. Limpinsel, Y. Liu, N. Farhi, A. Weber, Y. N. Zhang, N. Berry, Y. J. Kwon, C. L. Perkins, J. C. Hemminger, R. Q. Wu and M. Law, *J Am Chem Soc*, 2013, **135**, 4412-4424.
2. C. Steinhagen, T. B. Harvey, C. J. Stolle, J. Harris and B. A. Korgel, *J Phys Chem Lett*, 2012, **3**, 2352-2356.
3. L. K. Ganta, T. P. Dhakal, S. Rajendran and C. R. Westgate, *Mater. Res. Soc. Symp. Proc.*, 2012.
4. A. Kirkemide, R. Scott and S. Q. Ren, *Nanoscale*, 2012, **4**, 7649-7654.
5. J. Hu, Y. N. Zhang, M. Law and R. Q. Wu, *J Am Chem Soc*, 2012, **134**, 13216-13219.
6. T. P. Dhakal, L. K. Ganta, D. Vanhart, C. R. Westgate and Ieee, *Annealing of FeS₂ Nano-crystal Thin Film*, 2012.
7. L. Vadkhiya and B. L. Ahuja, in *Solid State Physics: Proceedings of the 55th Dae Solid State Physics Symposium 2010, Pts a and B*, eds. A. B. Garg, R. Mittal and R. Mukhopadhyay, 2011, pp. 1071-1072.
8. F. Alharbi, J. D. Bass, A. Salhi, A. Alyamani, H. C. Kim and R. D. Miller, *Renew Energ*, 2011, **36**, 2753-2758.
9. B. Meester, L. Reijnen, A. Goossens and J. Schoonman, *Chemical Vapor Deposition*, 2000, **6**, 121-128.
10. A. Ennaoui, S. Fiechter, C. Pettenkofer, N. Alonsovante, K. Buker, M. Bronold, C. Hopfner and H. Tributsch, *Sol Energ Mat Sol C*, 1993, **29**, 289-370.
11. A. Ennaoui, S. Fiechter, W. Jaegermann and H. Tributsch, *Journal of the Electrochemical Society*, 1986, **133**, 97-106.
12. J. Puthussery, S. Seefeld, N. Berry, M. Gibbs and M. Law, *J Am Chem Soc*, 2010, **133**, 716-719.
13. J. Joo, H. B. Na, T. Yu, J. H. Yu, Y. W. Kim, F. X. Wu, J. Z. Zhang and T. Hyeon, *J Am Chem Soc*, 2003, **125**, 11100-11105.
14. H. A. Macpherson and C. R. Stoldt, *Acs Nano*, 2012, **6**, 8940-8949.
15. M. G. Gong, A. Kirkemide and S. Q. Ren, *Sci Rep-Uk*, 2013, **3**.
16. Y. X. Bai, J. Yeom, M. Yang, S. H. Cha, K. Sun and N. A. Kotov, *J Phys Chem C*, 2013, **117**, 2567-2573.
17. B. Oregan and M. Gratzel, *Nature*, 1991, **353**, 737-740.
18. S. Ito, T. N. Murakami, P. Comte, P. Liska, C. Gratzel, M. K. Nazeeruddin and M. Gratzel, *Thin Solid Films*, 2008, **516**, 4613-4619.
19. A. Yella, H. W. Lee, H. N. Tsao, C. Y. Yi and A. K. Chandiran, *Science*, 2011, **334**, 1203-1203.
20. W. Chen, Y. C. Qiu, K. Y. Yan and S. H. Yang, *J Power Sources*, 2011, **196**, 10806-10816.
21. K. Y. Yan, Y. C. Qiu, W. Chen, M. Zhang and S. H. Yang, *Energy & Environmental Science*, 2011, **4**, 2168-2176.
22. K. P. Guo, K. Y. Yan, X. Q. Lu, Y. C. Qiu, Z. K. Liu, J. W. Sun, F. Yan, W. Y. Guo and S. H. Yang, *Org Lett*, 2012, **14**, 2214-2217.
23. Y. C. Qiu, W. Chen and S. H. Yang, *Angew Chem Int Edit*, 2010, **49**, 3675-3679.
24. J. D. Roy-Mayhew, G. Boschloo, A. Hagfeldt and I. A. Aksay, *Acs Appl Mater Inter*, 2012, **4**, 2794-2800.
25. L. Kavan, J. H. Yum, M. K. Nazeeruddin and M. Gratzel, *Acs Nano*, 2011, **5**, 9171-9178.
26. M. X. Wu, X. Lin, T. H. Wang, J. S. Qiu and T. L. Ma, *Energy & Environmental Science*, 2011, **4**, 2308-2315.
27. J. Zhang, T. Hreid, X. Li, W. Guo, L. Wang, X. Shi, H. Su and Z. Yuan, *Electrochimica Acta*, 2010, **55**, 3664-3668.
28. H. Wang, Q. Y. Feng, F. Gong, Y. Li, G. Zhou and Z. S. Wang, *J Mater Chem A*, 2013, **1**, 97-104.
29. M. X. Wu, X. Lin, Y. D. Wang, L. Wang, W. Guo, D. D. Qu, X. J. Peng, A. Hagfeldt, M. Gratzel and T. L. Ma, *J Am Chem Soc*, 2012, **134**, 3419-3428.
30. F. Gong, H. Wang, X. Xu, G. Zhou and Z. S. Wang, *J Am Chem Soc*, 2012, **134**, 10953-10958.
31. M. Wu, X. Lin, A. Hagfeldt and T. Ma, *Angew Chem Int Ed Engl*, 2011, **50**, 3520-3524.
32. M. K. Wang, A. M. Anghel, B. Marsan, N. L. C. Ha, N. Pootrakulchote, S. M. Zakeeruddin and M. Gratzel, *J Am Chem Soc*, 2009, **131**, 15976-+.
33. L. X. Yi, Y. Y. Liu, N. L. Yang, Z. Y. Tang, H. J. Zhao, G. H. Ma, Z. G. Su and D. Wang, *Energy & Environmental Science*, 2013, **6**, 835-840.
34. Y. C. Wang, D. Y. Wang, Y. T. Jiang, H. A. Chen, C. C. Chen, K. C. Ho, H. L. Chou and C. W. Chen, *Angew Chem Int Edit*, 2013, **52**, 6694-6698.
35. Z. Wei, Z. Zhou, M. Yang, C. Lin, Z. Zhao, D. Huang, Z. Chen and J. Gao, *J Mater Chem*, 2011, **21**, 16344-16348.
36. J. H. Gao, G. L. Liang, B. Zhang, Y. Kuang, X. X. Zhang and B. Xu, *J Am Chem Soc*, 2007, **129**, 1428-1433.
37. J. Gao, G. Liang, J. S. Cheung, Y. Pan, Y. Kuang, F. Zhao, B. Zhang, X. Zhang, E. X. Wu and B. Xu, *J Am Chem Soc*, 2008, **130**, 11828-11833.
38. G. J. Cheng, D. Romero, G. T. Fraser and A. R. H. Walker, *Langmuir*, 2005, **21**, 12055-12059.
39. J. Huang, W. M. Chen, W. Zhao, Y. Q. Li, X. G. Li and C. P. Chen, *J Phys Chem C*, 2009, **113**, 12067-12071.
40. J. H. Gao, B. Zhang, X. X. Zhang and B. Xu, *Angew Chem Int Edit*, 2006, **45**, 1220-1223.
41. H. L. Niu, Q. W. Chen, H. F. Zhu, Y. S. Lin and X. Zhang, *J Mater Chem*, 2003, **13**, 1803-1805.
42. L. Guo, F. Liang, X. Wen, S. Yang, L. He, W. Zheng, C. Chen and Q. Zhong, *Adv Funct Mater*, 2007, **17**, 425-430.
43. G. Boschloo, J. Lindstrom, E. Magnusson, A. Holmberg and A. Hagfeldt, *J Photochem Photobiol A*, 2002, **148**, 11-15.
44. T. Yamaguchi, N. Tobe, D. Matsumoto and H. Arakawa, *Chem Commun*, 2007, 4767-4769.



32x13mm (300 x 300 DPI)